Structural and thermoelastic study of the protonic conducting perovskite SrCe$_{0.95}$Yb$_{0.05}$O$_\xi$ (ξ~3) between 373 K and 1273 K

Kevin S. Knight

Abstract The temperature dependence of the crystal structure of the protonic conducting perovskite SrCe$_{0.95}$Yb$_{0.05}$O$_\xi$ (ξ~3) has been determined from Rietveld refinement of neutron time-of-flight powder diffraction data in 25 K steps from 373 K to 1273 K. In contrast to most SrB^{IV}O$_3$ perovskites which show a sequence of structural phase transitions from *Pmcn – Incn – I4/mcm - Pm$\overline{3}$m* with increasing temperature, SrCe$_{0.95}$Yb$_{0.05}$O$_\xi$ remains orthorhombic with space group *Pmcn* from 4.2 K to the highest temperature measured. Crystallographic results are presented graphically in the form of the magnitude of the seven unique symmetry adapted basis vectors of a hypothetical aristotype perovskite phase. Thermoelastic properties of SrCe$_{0.95}$Yb$_{0.05}$O$_\xi$ deduced from the temperature variation of the unit cell volume and Debye-Waller factors are compared with literature values derived from independent calorimetric, Raman and elastic measurements. Thermodynamically, SrCe$_{0.95}$Yb$_{0.05}$O$_\xi$ behaves as a Debye-like solid with an average Grüneisen parameter in the range 1.4–1.5, but with two characteristic temperatures, ~200 K and ~600 K, the lower temperature being more related to the cation vibrations, the higher to the anion vibrations.

K. S. Knight (✉)
ISIS Facility, STFC Rutherford Appleton Laboratory,
Harwell Oxford,
Didcot, Oxon OX11 0QX, UK
e-mail: kevin.knight@stfc.ac.uk

K. S. Knight
Department of Mineralogy, The Natural History Museum,
Cromwell Road,
London SW7 5BD, UK

1 Introduction

A number of high temperature proton conductors have been investigated over the past 30 years, including the perovskite-structured phases SrCeO$_3$, BaCeO$_3$, SrZrO$_3$ and BaZrO$_3$ with potential application as electrolytes for solid oxide fuel cells, water electrolysers, gas sensors and ceramic electrochemical reactors. In most investigations, these compounds (ABO$_3$) are doped with trivalent cations substituting on the octahedrally-coordinated, tetravalent B site resulting in an anion deficient phase i.e. they contain extrinsic vacancies. Among these compounds, Yb-doped SrCeO$_3$ has received a great deal of attention because of its high protonic conductivity in the temperature range 873–1273 K combined with relatively low oxide ion conductivity [1].

The hydrogen-containing species in these perovskite-structured compounds are in fact hydroxyl ions, formed by absorption of water vapour from the surroundings, with ionic transport occurring by protons hopping between oxygen ions. According to the reaction below (written in Kröger-Vink notation), oxygen vacancies are required for the water vapour dissolution; hence the preference for acceptor doped systems.

$$H_2O + V_O^{\bullet\bullet} + O_o^\times \rightarrow 2\,OH_O^\bullet$$
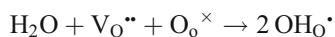
Given the large number of potential host and dopant systems available, efforts have been made to understand the thermodynamics of hydration in terms of the structure and chemistry of the oxides. Kreuer et al. [2] identified the basicity of the cations as affecting the hydration enthalpy, while Norby et al. [3] focused on the weighted average electronegativity of the cations. In particular, Norby et al. pointed out that the hydration enthalpy correlated with the difference in weighted average electronegativities of the A-

and B-site occupying ions. By contrast, the hydration entropy does not differ greatly from one oxide system to another, and hence mainly represents the loss of the entropy of the water vapour molecule. The dynamics of the oxygen sublattice has been found to affect the rate of proton transport, and, contrary to expectation, long metal-oxygen bond lengths favour high hopping rates, as they permit large vibrations/librations of the oxygen ions within the B-site octahedron [2]. Finally, the existence of more than one crystallographically distinct oxygen site in systems of low crystallographic symmetry, potentially allows an ordering of the dopant-induced vacancies [4, 5], which could result in trapping of mobile protons. Thus, the crystal symmetry and unit cell volume affect both the thermodynamics and kinetics of protonic defects in oxides.

The crystal structure of $SrCeO_3$ was first determined by Saiki et al. [6] from a Rietveld refinement of powder X-ray diffraction data, and a higher precision structure was subsequently, and independently, determined by Knight and Bonanos using time-of-flight, powder neutron diffraction data [7]. In this same publication, the crystal structure of $SrCe_{0.95}Yb_{0.05}O_\xi$, determined at room temperature, was also reported in the orthorhombic space group $Pmcn$. The extrinsic vacancy introduced on doping with the aliovalent Yb could not be located in this study in contrast to work carried out on Nd- and Y-doped $BaCeO_3$ [4, 5], and in this high-temperature investigation it has been assumed that the vacancy is statistically distributed over both crystallographically independent oxygen sites.

In recent years there has been a renaissance in the crystallographic studies of perovskite phase transitions, in part due to the increased availability of high-resolution diffractometers which are necessary to resolve the small ferroelastic strains that accompany these transitions. Based on a high-resolution, time-of-flight, powder neutron diffraction study, the structural phase transitions in the archetype perovskite $SrZrO_3$ were correctly characterised for the first time as being $Pnma – Imma – I4/mcm - Pm\overline{3}m$ (all standard settings of the space groups) [8]. Subsequent work on similar $SrB^{IV}O_3$ systems showed that this sequence of structural phase transitions appeared to be the norm, being found in $SrRuO_3$ [9], $SrRhO_3$ [10], $SrSnO_3$ [11], $SrHfO_3$ [12] and $Sr_{1-x}Ba_xZrO_3$ [13]. Only $SrPbO_3$ showed the absence of any high-temperature phase transition, a situation which Knight et al. attributed to the Pb – O bond length exceeding a limiting bond length for stabilizing the aristotype structure [14]. As the Ce – O bond length is also long when compared to the equivalent octahedrally-coordinated metal – oxygen bond lengths in the Ru/Rh/Sn/Hf/Zr perovskite phases, the high-temperature crystal structure of $SrCe_{0.95}Yb_{0.05}O_\xi$ has been investigated to see whether it also behaves in the anomalous manner of $SrPbO_3$. In addition to structural characterization, results

from this investigation have been used to supplement the poorly known thermoelastic properties of the $A^{II}B^{IV}O_3$ perovskite family.

2 Experimental, data reduction and data analysis

The sample of $SrCe_{0.95}Yb_{0.05}O_\xi$ was prepared by solid state reaction of $SrCO_3$, CeO_2 and Yb_2O_3 powders. Starting materials were dried at 400°C, mixed in the correct stoichiometric proportions, pre-reacted at 1000°C and then ground and refired at 1200°C and then again at 1400°C for several days. Finally the product was ground to <100 μm and fired at 600°C to remove any residual strain in the sample. All firings were carried out in air.

Powder neutron diffraction data were collected on the POLARIS diffractometer of the ISIS pulsed neutron source at the Rutherford Appleton Laboratory (RAL) UK. 3.8 cm^3 of sample (~7.1 g) was contained in an 11 mm diameter, thin-walled vanadium sample can and attached to the centre stick of an RAL vacuum furnace with the tip of the furnace control thermocouple attached to the body of the sample can approximately 2.5 cm above the neutron beam centre. The sample temperature was controlled at each temperature to better than ±0.5 K. For the first temperature (373 K) the sample was heated to the set point and the furnace was allowed to out-gas and equilibrate for 1 h before data collection was commenced. Data were collected at 373 K and in 25 K steps to the maximum temperature of 1273 K with data collection times being alternated between 180 μAh and 45 μAh incident proton beam current. The raw data from the back-scattering detectors were focused, background subtracted and normalized to a vanadium standard to correct for the incident flux distribution and wavelength-dependent detector efficiencies. Finally the data were corrected for self-shielding and wavelength-dependent absorption for a sample with ideal stoichiometry, measured number density of 4.04×10^{21} cm^{-3}, scattering cross section of 22.8 b, and an absorption cross section of 3.6 b at a wavelength of 1.798 Å. Data in the time-of-flight range 2.0 ms–19.5 ms (~0.32 Å–3.16 Å range in d-spacing), binned logarithmically at $\Delta T/T = 0.0005$, were used in profile refinement. The GSAS package was used for all structure refinements [15].

Convergence of the 373 K refinement from the ambient temperature structural coordinates of $SrCe_{0.95}Yb_{0.05}O_\xi$ [7] was rapid, with the results from this refinement being used as a seed for the subsequent data set, the process being iterated until the highest temperature data set was completed. Anisotropic atomic displacement parameters were only found to be statistically significant for the two anion sites; the two cations were therefore refined with isotropic atomic displacement parameters. Representative results from these refine-

ments (unit cell, structural and atomic displacement parameters and profile agreement factors) are shown in Table 1. Full crystallographic results at each of the thirty-seven temperatures are available as supplementary data. An example of a typical fit to the 180 μAh data is shown in Fig. 1.

To avoid potential ambiguity in the labeling of the anions, in Table 1, and in the subsequent discussion of the crystal structure, the two independent oxygen sites are designated O1 and O2, whilst in the discussion of the symmetry adapted basis vector decomposition of the space group, the three anion positions in the (hypothetical) aristotype phase of $SrCe_{0.95}Yb_{0.05}O_\xi$ are labelled O_I, O_{II} and O_{III}. O1 is derived from O_{III}, while O2 is derived from both O_I and O_{II} (see section 3.4 for a detailed explanation).

3 Results and discussions

3.1 Unit cell volume and Grüneisen parameter

Our unpublished low-temperature measurements of $SrCe_{0.95}Yb_{0.05}O_\xi$ have shown that it is orthorhombic, space group *Pmcn* at 4.2 K, and inspection of the temperature-dependence of the diffraction patterns in this high-temperature study showed no evidence for the presence structural phase transitions between room temperature and

Fig. 1 Rietveld fit to $SrCe_{0.95}Yb_{0.05}O_\xi$ for data collected at 373K with the quality of the high $\frac{\sin(\theta)}{\lambda}$ region of the diffraction pattern shown as an inset. Observed (•), calculated (−) and difference (bottom)

1273K. In zone-boundary tilted perovskite-structures, with increasing temperature these would be evident as the systematic disappearance of superlattice reflections at the M or the R point of the pseudocubic Brillouin zone. Superlattice reflections at the X point are only present when both M and R point superlattice reflections are also present, and disappear with increasing temperature when either the M point or R point superlattice reflections are lost. $SrCe_{0.95}Yb_{0.05}O_\xi$ hence appears to be similar to $SrPbO_3$ in that the magnitude of the Ce - O bond length results in an aristotype Sr – O bond length that greatly exceeds the limiting value of ~3.0 Å [14].

Figure 2 shows the variation of the unit-cell volume with temperature and indicates that the temperature-dependence is nonlinear with a smooth upward trend that is most visible at high temperatures. Fitting these data to a weighted second-order polynomial gave the following expression for the unit cell volume as a function of temperature:

$$V(T) = 313.43(4) + 7.4(1) \times 10^{-3}T + 2.30(1) \times 10^{-6}T^2$$

which is shown as the full line on the figure. At 373K the volume expansion coefficient is $2.88(1) \times 10^{-5}$ K^{-1}, and increases to $4.06(2) \times 10^{-5}$ K^{-1} by 1273 K; these values

Table 1 Structural Parameters for $SrCe_{0.95}Yb_{0.05}O_\xi$ at three representative temperatures. Sr 4c (1/4, y, z), Ce 4a (0, 0, 0), O1 4c (1/4, y, z), O2 8d (x, y, z)
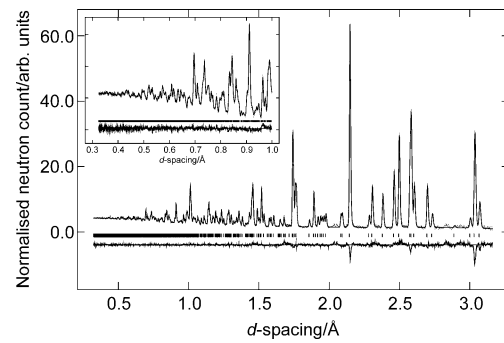
		373K	723K	1273K
Sr	y	0.5118(2)	0.5102(2)	0.5063(4)
	z	−0.0433(1)	−0.0391(1)	−0.0296(3)
	$100u_{iso}$/Å^2	0.82(1)	1.86(2)	3.90(4)
Ce	$100u_{iso}$/Å^2	0.47(1)	0.93(2)	1.80(3)
O1	y	0.1043(2)	0.0995(3)	0.0890(4)
	z	0.0421(2)	0.0391(3)	0.0308(5)
	$100u_{eq}$/Å^2	0.82(4)	1.99(7)	4.36(16)
O2	x	−0.0553(1)	−0.0522(1)	−0.0457(2)
	y	0.2001(1)	0.2002(2)	0.2036(3)
	z	0.2993(1)	0.2991(2)	0.2976(3)
	$100u_{eq}$/Å^2	1.13(3)	2.31(5)	5.05(10)
a/Å		8.5816(1)	8.6187(1)	8.6841(2)
b/Å		6.00611(7)	6.03769(8)	6.0997(1)
c/Å		6.14021(8)	6.14881(9)	6.1654(1)
χ^2		1.27	0.98	1.12

$\chi^2 = \left(R_{wp}/R_E\right)^2$

$R_{wp} = \left\{ \sum w_i [(y_i(obs) - y_i(calc)]^2 / \sum w_i y_i(obs)^2 \right\}^{0.5}$

$R_E = \left\{ [N - P + C] / \sum w_i y_i(obs)^2 \right\}^{0.5}$

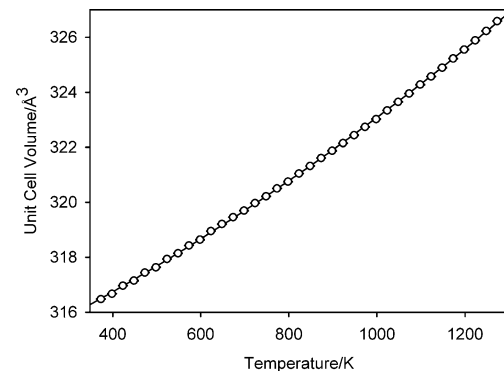where N, P, C are the numbers of observations, parameters and constraints respectively

Fig. 2 The temperature dependence of the unit cell volume of $SrCe_{0.95}Yb_{0.05}O_\xi$ with a second-order polynomial least-squares fit to the data shown as a full line

bracket three times the average linear thermal expansion coefficient of SrCeO$_3$ measured by dilatometry over the identical temperature interval [17].

Assuming a Debye internal energy function and a Grüneisen approximation to the zero-pressure equation of state [18], to first order the unit-cell volume scales with internal energy

$$V(T) = V_0 + \frac{9\gamma N K_B T}{B_0} \left(\frac{T}{\Theta_D}\right)^3 \int_0^{\Theta_D/T} \frac{x^3}{e^x - 1} dx$$

where γ is a Grüneisen parameter, θ_D is the Debye temperature, N is the number of atoms in volume V$_0$, B$_0$ is the isothermal bulk modulus and K$_B$ is Boltzmann's constant. The lack of a significant linear region in the temperature-dependence of the unit cell volume however precluded fitting these data to this expression, and physically unrealistic Debye temperatures were always derived. However, refitting the temperature variation of the unit cell volume to a straight line, and assuming the bulk modulus of SrCe$_{0.95}$Yb$_{0.05}$O$_\xi$ was identical to that of SrCeO$_3$, the high-temperature limit of the integral allows an estimation to be made of the Grüneisen parameter, γ,

$$\gamma = \frac{B_O}{3NK_B} \frac{dV}{dT}$$

where B$_0$=1.101×10^{11} Pa [14] ,$\frac{dV}{dT} = 1.115 \times 10^{-32}$ m^{3}K^{-1}, and $\gamma \sim 1.48$. This estimated value can be directly compared with the thermodynamic Grüneisen parameter γ_{th} determined from measurements of the heat capacity, bulk modulus and volume expansivity,

$$\gamma_{th}(T) = \frac{\alpha(T) B_0(T) V_m(T)}{Cv(T)}$$

where V$_m$ is the molar volume, B$_0$ is the isothermal bulk modulus (assumed temperature independent), α is the volume thermal expansion coefficient and Cv is the molar isochoric specific heat. Converting the values of the isobaric heat capacity (Cp), obtained in the recent calorimetric study of SrCeO$_3$ [19], to the isochoric heat capacity (Cv=Cp - TK$_0\alpha^2$V$_m$), γ_{th}(T) was calculated using the expression above. Figure 3 shows the temperature dependences of the isochoric heat capacity and the thermodynamic Grüneisen parameter between 298 K and 900 K. The thermodynamic Grüneisen parameter varies from 1.35 to 1.53 within this temperature range, with $\overline{\gamma_{th}(T)} = 1.41$, close to the value estimated from the volume expansivity. Further evidence for an average Grüneisen parameter of ~1.4–1.5 for SrCe$_{0.95}$Yb$_{0.05}$O$_\xi$ can be found by analyzing the mode Grüneisen parameters of the SrO$_8$ polyhedron in SrCeO$_3$ determined by high-pressure Raman Spectroscopy [20]. Using the directly measured value of the polyhedral
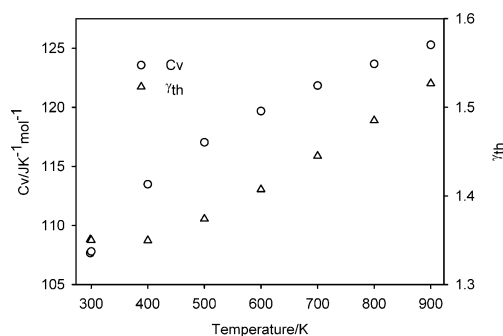
Fig. 3 The temperature dependence of the isochoric heat capacity (circles) for SrCeO$_3$ and the calculated thermodynamic Grüneisen parameter (triangles) for SrCe$_{0.95}$Yb$_{0.05}$O$_\xi$ based on these data

compressibility of the SrO$_8$ polyhedron of 8.7×10^{-12} Pa^{-1} [14], the mode Grüneisen parameters of the bands that occur at 119.5 cm^{-1} and 113 cm^{-1} at ambient pressure are 1.40 and 1.44 respectively.

The range in values for the thermodynamic Grüneisen parameter for SrCe$_{0.95}$Yb$_{0.05}$O$_\xi$ are in good agreement with the spread of values of the ambient temperature Grüneisen parameter calculated for other A^{II}B^{IV}O$_3$ perovskites using the linear thermal expansion coefficients, unit cell volumes and bulk moduli quoted in Yamanaka et al. [21]: BaHfO$_3$ (0.83), BaSnO$_3$ (1.37), BaZrO$_3$ (0.97), BaUO$_3$ (0.99), BaCeO$_3$ (1.92), BaMoO$_3$ (1.39), SrHfO$_3$ (1.27), SrRuO$_3$ (1.56), SrMoO$_3$ (1.06) and SrCeO$_3$ (0.81). Note that the bulk modulus of SrCeO$_3$ determined by Yamanaka et al. is significantly different from that derived from the equation of state [14]; substituting for this value gives a Grüneisen parameter for SrCeO$_3$ of 1.39, in agreement with the values determined by calorimetry, volume expansivity and Raman spectroscopy.

3.2 Unit-cell metric

Further evidence for the lack of structural phase transitions over the temperature range investigated can be seen in the smooth, non-linear temperature variation of the orthorhombic unit cell parameters, shown in Fig. 4(a), which have been empirically fitted to second order polynomials:

$$a(T) = 8.5461(2) + 9.01(7) \times 10^{-5}T + 1.42(4) \times 10^{-8}T^2$$

$$b(T) = 5.9791(2) + 6.34(4) \times 10^{-5}T + 2.48(3) \times 10^{-8}T^2$$

$$c(T) = 6.1337(2) + 1.56(5) \times 10^{-5}T + 6.55(3) \times 10^{-9}T^2.$$

The temperature dependence of the monoclinic, pseudocubic unit cell, subscripted p, (transformation from the *Pmcn* orthorhombic cell: 1/2 0 0/0 1/2 -1/2/0 1/2 1/2; b$_p$= c$_p \neq$ a$_p$, $\alpha_p \neq 90°$) is shown in Fig. 4(b), and shows that while the pseudocubic a axis and the b/c axes cross at around 700
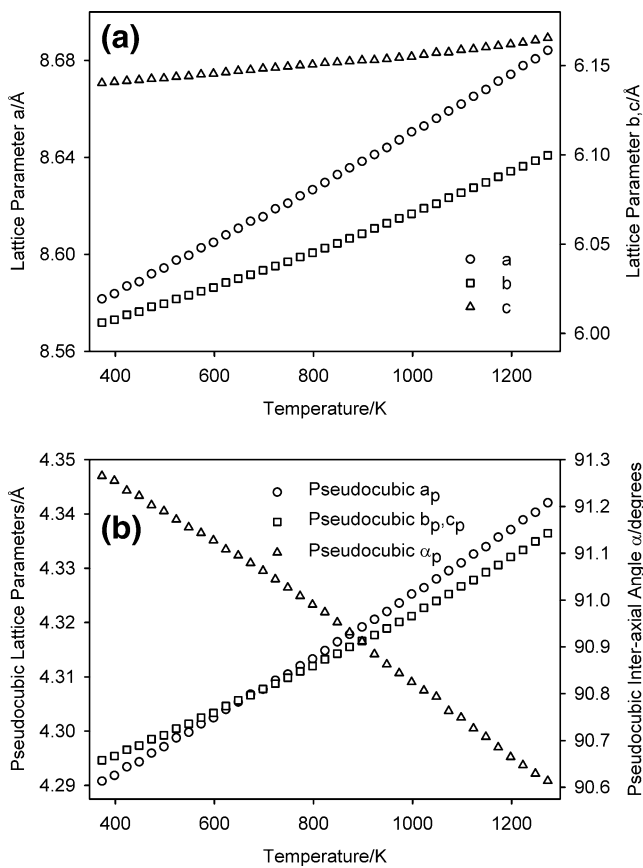
Fig. 4 (**a**) The temperature dependence of the orthorhombic unit cell parameters. (**b**) The temperature dependence of the associated pseudocubic lattice parameters

where it can be seen to a good approximation that $\frac{1}{b_0}\frac{db}{dT} \approx \frac{1}{a_0}\frac{da}{dT} + \frac{1}{c_0}\frac{dc}{dT}$. For a perovskite in space group *Pmcn* this solution is exact for the special case of an ideal, regular octahedron, and can be derived directly from the expressions given by O' Keefe and Hyde [22] for the magnitudes of the unit cell edges that results from the rotation of the octahedron around the [111] direction of the aristotype phase. This experimental observation is not a common occurrence however, and arises in this particular case from the regularity of the B-site octahedron in $SrCe_{0.95}Yb_{0.05}O_{\xi}$, and, perhaps more importantly, the lack of a structural phase transition in the temperature interval that was measured. This result is approximately obeyed in $SrPbO_3$, which like $SrCeO_3$ shows no temperature-induced structural phase transitions up to 1033K [23] and for $NaMgF_3$ between 298K and 873K [24] i.e. well below the *Pmcn* − *P4/mbm* phase transition.

3.3 Atomic displacement parameters and vibrational characteristic temperatures

The temperature variation of the isotropic/isotropic equivalent atomic displacement parameters for the two cations and the two symmetry independent anions are shown in Fig. 5. Consideration of this figure shows that the temperature variation of the isotropic displacement parameter of the Sr cation is almost identical to that of the equivalent isotropic displacement parameter for O1; both atoms lying on the mirror plane in the crystal structure. The temperature dependence of the equivalent isotropic displacement parameter for O2 is close to both that of O1 and the A site, while that of the octahedral site Ce/Yb shows a markedly different gradient. Since Rietveld refinement only

K, the monoclinic pseudocubic shear angle remains large and non-ninety degrees up to the highest temperature measured. Both the conventional and pseudocubic unit cells indicate the lack of structural phase transitions up to 1273 K in agreement with the calorimetric measurements [19]. Fitting the temperature-dependence of the pseudocubic shear angle to a quadratic function of temperature suggests that a phase transition might occur in the vicinity of 1886 K when α_p extrapolates to 90°. However, these extrapolations are generally unreliable, and data at significantly higher temperatures would be required to give confidence in the estimation of a potential structural phase transition temperature.

The average axial thermal expansion coefficients, determined from fitting the conventional lattice parameter data to a straight line, gives values of

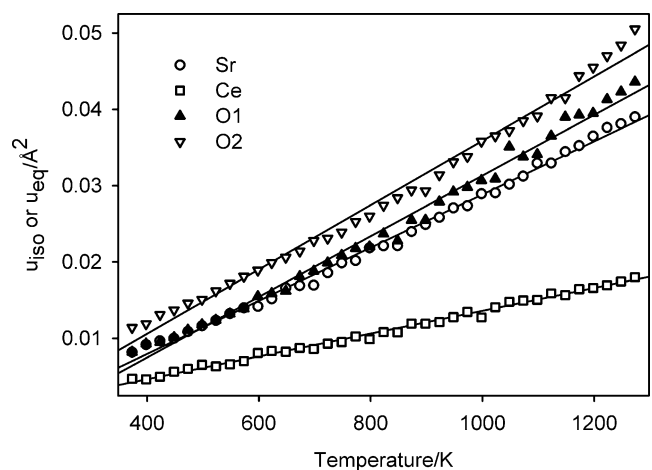$$\frac{1}{a_0}\frac{da}{dT} = 1.320(1) \times 10^{-5}K^{-1}$$

$$\frac{1}{b_0}\frac{db}{dT} = 1.732(1) \times 10^{-5}K^{-1}$$

$$\frac{1}{c_0}\frac{dc}{dT} = 4.26(1) \times 10^{-6}K^{-1}$$

Fig. 5 The temperature dependence of the isotropic, atomic displacement parameters for Sr and Ce/Yb and the temperature variation of the equivalent isotropic atomic displacement parameters for O1 and O2. Straight lines show the least-squares fits to a modified Debye model for the temperature variation of the atomic displacement parameters

uses Bragg reflections to derive structural information, it is formally invalid to draw any conclusions about pair correlations of atomic motions; nonetheless, this result is highly suggestive that the motion of the A-site cation is influenced by the temperature dependence of the librational optic modes arising from the un-tilting of the essentially rigid octahedron. This point will be returned to in the discussion of the effect of temperature on the crystal structure.

Following James [25], the temperature-dependence of the atomic displacement parameter in the Debye approximation is given by

$$\overline{u^2}(T) = \frac{145.55T}{M\Theta_D^2}\left(\frac{T}{\Theta_D}\int_0^{\Theta_D/T}\frac{x}{e^x-1}dx\right) + \frac{36.39}{M\Theta_D}$$

where M is the mass of the vibrating atom and θ_D is the vibrational Debye temperature. For temperatures significantly greater than the vibrational Debye temperature this expression simplifies to

$$\overline{u^2}(T) = \frac{145.55T}{M\Theta_D^2},$$

with the atomic displacement parameter linear in temperature [26]. In Fig. 5, straight line fits to the atomic displacement parameters for all atoms are shown, where they can be seen to fit both cations species acceptably well but the fit is significantly poorer in the case of the two anions. This is probably related to the isotropic averaging of an intrinsically anisotropic displacement parameter in which the degree of anisotropy is strongly temperature dependent. In addition, an extra offset constant term in the expression has been introduced, i.e. the fitted lines do not pass through the origin as the high-temperature limit of the Debye function requires, as this is found to place too great a constraint to be physically realistic. From the gradients of the fitted straight lines, the vibrational Debye temperatures have been determined as: Sr 222(1) K, Ce/Yb 265(2) K, O1 494(4) K and O2 479(3) K where there is a clear difference between the characteristic temperatures associated with the anions and cations.

Figure 6 shows the experimentally determined low temperature isobaric heat capacity data of SrCeO$_3$ [19] and two fits to the data according to an isochoric Debye heat capacity, noting that the difference between Cp and Cv is essentially negligible at low temperature. For a Debye solid, the isochoric heat capacity is given by

$$C_v(T) = 9NK_BT\left(\frac{T}{\Theta_D}\right)^3\int_0^{\Theta_D/T}\frac{x^4 e^x}{(e^x-1)^2}dx$$

with the dot-dash line in the figure showing the results of a least-squares fit to the heat capacity data, from which the
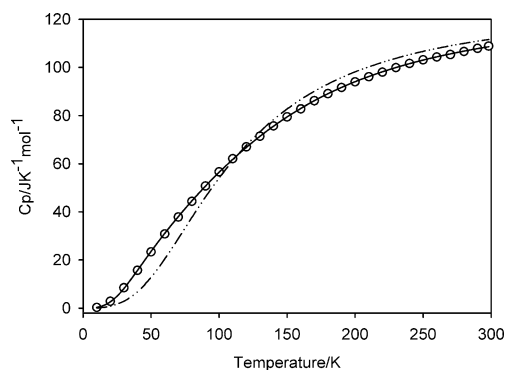
Fig. 6 The low-temperature isobaric heat capacity of SrCeO$_3$. The dot-dash line shows the results of a least-squares fit to the isochoric heat capacity using a Debye model for the vibrational density of states. The full line shows the results of fitting the two Debye moment model (described in detail in section 3.3) to the experimental data

Debye temperature was estimated to be 449(8) K. Consideration of the figure shows that at low temperatures the observed heat capacity is greater than that calculated, showing that SrCeO$_3$ has more active modes than that predicted by a Debye model. At high temperatures the opposite effect is found, indicating that there are significantly fewer active modes than the Debye model predicts. The solid line in the Fig. 6 shows the results of fitting the more sophisticated Debye model of Barron [27] which is composed of the sum of two independent isochoric specific heat contributions, Cv$_i$(E$_i$), that allows different cut-off frequencies for the longitudinal and transverse modes.

$$C_v(T) = \frac{1}{3}C_{v1}(T) + \frac{2}{3}C_{v2}(T).$$

The fit to this model is excellent with the characteristic temperatures θ_{D1}=206(6) K and θ_{D2}=604(7) K. Equally good fits were found for the sum of two independent Einstein oscillator heat capacities, or a mixture of a Debye model for the lower characteristic temperature, with an Einstein oscillator contribution for the higher characteristic temperature. Although the fit to the isochoric heat capacity is good, there remains a significant problem with the results derived from fitting the Barron model to the data. The expectation that the energy of the longitudinal mode would be higher than that of the two degenerate transverse modes is not found, and hence we interpret the heat capacity results in terms of a phonon density of states having the form of the sum of two separate Debye functions rather than the modified Debye model of Barron [27]. Retaining this two-Debye-moment-model, it is clear that the lower characteristic temperature is close to the experimentally determined vibrational Debye temperatures for the cations, whilst the higher characteristic temperature is similar to that determined for the two anions.

The consistency of the vibrational Debye temperatures from the high-temperature crystallographic study with the characteristic temperatures derived from fitting the low-temperature heat capacity measurements suggests that $SrCe_{0.95}Yb_{0.05}O_\xi$ can be considered thermodynamically as a modified Debye-like solid. The possibility of treating a perovskite-structured phase in a strict Debye model has been discussed earlier by Anderson for the geophysical implications of the high-temperature/high-pressure behaviour of the isostructural, mantle perovskite phase $MgSiO_3$ [28]. Whether $MgSiO_3$ behaves as a true Debye solid as envisaged by Anderson, or whether it behaves like $SrCe_{0.95}Yb_{0.05}O_\xi$, remains to be experimentally verified.

3.4 The temperature-dependence of the crystal structure of $SrCe_{0.95}Yb_{0.05}O_\xi$

Knight has recently published a method for decomposing the crystal structures of centrosymmetric zone-boundary tilted perovskites [29] and elpasolites [30] in terms of the magnitudes of the symmetry adapted basis vectors of the cubic aristotype phase. The advantages of such a decomposition are two-fold; firstly, the magnitude of the primary order parameters, the in-phase and anti-phase tilts, are determined exactly without trigonometric approximation; secondly, the degrees of freedom required by the derived crystal structure (subject to quality of the data), rather than those imposed by space group symmetry, can be determined directly. Finally, if the dependences of the mode amplitudes and the unit cell parameters as a function of applied thermodynamic variable can be simply parameterized, it is possible to predict the evolution of the bond lengths and bond angles in any coordination shell [31]. Both methods of analysis require equally precise coordinates for the A site and the anions and are unlikely to give reliable results for heavy atom A and B site oxide perovskite crystal structures refined from X-ray powder diffraction data.

Table 2 shows the symmetry adapted basis vectors determined by Cowley for the aristotype phase [16] but transformed to be consistent with the space group setting *Pmcn*. Modes in bold italics form the displacements associated with the primary order parameters (the in-phase and two equal anti-phase tilts) in this space group, modes in italics form the displacements associated with the secondary order parameters. The seven spatial degrees of freedom associated with a centrosymmetric perovskite in space group *Pmcn* gives rise to seven symmetry adapted basis vectors, labeled d_i ($i=1, 7$) in the Table. Note that the irreducible representations in this table use the notation of Miller and Love [32], and not the original labeling of Cowley [16].

Table 2 Symmetry adapted basis vector displacements for a perovskite-structured phase in space group *Pmcn*

Irreducible representation	Symmetry adapted basis vector		
$\zeta=(1/2\ 0\ 0)$			
X_3^-	B x	O_I x=O_{II} x	
X_1^+	A x	O_{III} x	
X_4^-	O_{II} x=$-O_I$ x		
X_5^-	B y	O_{II} y	O_I y
X_5^-	B z	O_{II} z	O_I z
X_5^+	*A y* (d$_2$)	*O_{III} y* (d$_5$)	
X_5^+	*A z* (d$_2$)	*O_{III} z* (d$_5$)	
$\zeta=(0\ 1/2\ 1/2)$			
M_4^+	O_{II} z=O_I y		
M_2^+	*O_I z=$-O_{II}$ y* (d$_6$)		
M_3^+	**O_{II} z=$-O_I$ y** (d$_4$)		
M_1^+	O_I z=O_{II} y		
M_2^-	A x		
M_3^-	B x	O_{III} x	
M_5^+	O_I x		
M_5^+	O_{II} x		
M_5^-	B y	A z	O_{III} y
M_5^-	B z	A y	O_{III} z
$\zeta=(1/2\ 1/21/2)$			
R_1^+	O_I z=O_{III} x=O_{II} y		
R_3^+	O_I z=O_{III} x=$-1/2\ O_{II}$ y		
R_3^+	O_{III} x=$-O_I$ z		
R_4^+	**O_I x=$-O_{III}$ z** (d$_3$)		
R_4^+	**O_{II} x=$-O_{III}$ y** (d$_3$)		
R_4^+	O_I y=$-O_{II}$ z		
R_4^-	B x		
R_4^-	B y		
R_4^-	B z		
R_5^+	A x	O_I y=O_{II} z	
R_5^+	*A y* (d$_1$)	*O_{III} z=O_I x* (d$_7$)	
R_5^+	*A z* (d$_1$)	*O_{II} x=O_{III} y* (d$_7$)	

The fractional coordinates for a perovskite in space group *Pmcn* in terms of the seven symmetry adapted basis vector magnitudes (d$_1$–d$_7$) are [29]:

$$A-\text{site}: \frac{1}{4}, \frac{1}{2}-\frac{\sqrt{2}d_1}{b}, \frac{\sqrt{2}d_2}{c}$$

$$B-\text{site}: 0, 0, 0$$

$$O1-\text{site}: \frac{1}{4}, \frac{\sqrt{2}(d_3-d_7)}{b}, \frac{\sqrt{2}d_5}{c}$$

$$O2-\text{site}: -\frac{(d_3+d_7)}{a}, \frac{1}{4}-\frac{(d_4-d_6)}{\sqrt{2}b}, \frac{1}{4}+\frac{(d_4+d_6)}{\sqrt{2}c}.$$

The orthogonal nature of the symmetry adapted basis vectors ensures that this solution is a unique description of

the crystal structure; see Perez-Mato et al. [33] for a clear and detailed review of the underlying group theory required for the mode decomposition of crystal structures. As an example, the magnitudes of these symmetry adapted basis vectors for the crystal structure of $SrCe_{0.95}Yb_{0.05}O_\xi$ at 373 K are listed in Table 3.

Figure 7 illustrates the bonding environment of the SrO_8 polyhedron in $SrCe_{0.95}Yb_{0.05}O_\xi$ viewed down $[0, -1, 1]$ with $[1, 0, 0]$ vertical. In this orientation, the nature of the anti-phase tilt can be readily appreciated in the left-hand pairs of octahedra. The effect of increasing temperature on the crystal structure is to decrease the magnitude of both the in-phase and the anti-phase tilts, albeit in a non-simple manner that arises from the potential coupling that is permitted between the two modes [34]. To a good approximation, the three independent Ce – O bond lengths and angles are found to exhibit little temperature variation, and hence the most significant structural changes occur in the SrO_8 polyhedron as it responds to the decreasing tilting displacement magnitudes.

The Sr cation lies on the mirror plane of the space group, and the figure shows that there are three crystallographically independent bonds to the anions O2, which lie off the mirror plane, and two independent bonds to O1 anions, which lie in the mirror plane. The SrO_8 polyhedron is characterised by three short Sr – O bonds of approximately 2.5Å in length, one to O1 (x1, y1-1/2, z1) and two to O2 (−x2, y2, 1/2-z2) and (1/2+x2, y2, 1/2-z2). The effect of temperature on these three contacts is to increase the bond lengths at approximately equal rates, 6.68×10^{-5} ÅK^{-1} for Sr - O1(3), and 7.31×10^{-5} ÅK^{-1} for Sr - O2(5), as shown in Fig. 8. Of the remaining five bonds, three are intermediate in length; one, approximately 2.6Å to O1(1) (x1, -y1, z1-1/2), and two at approximately 2.9 Å to O2(5) (−x2, 1/2-y2, -z2) and (1/2+x2, 1/2-y2, -z2). The final two distances are long at approximately 3.1Å to O2(3) (x2, -y2, z2-1/2) and (1/2-x2, -y2, z2-1/2). The displacement of the Sr cation from its ideal coordinate of (1/4, 0, 0) is principally along the orthorhombic z direction for which the condensed displacement magnitude, d_2, is greater than that

**Table 3** Displacement magnitudes of the symmetry adapted basis vectors in $SrCe_{0.95}Yb_{0.05}O_\xi$ at 373K

| Condensed mode	Magnitude/Å
$(R_5^+) d_1$	(−)0.050(1)
$(X_5^+) d_2$	(−)0.188(1)
$(R_4^+) d_3$	0.459(1)
$(M_3^+) d_4)$	0.426(1)
$(X_5^+) d_5$	0.183(1)
$(M_2^+) d_6$	0.002(1)
$(R_5^+) d_7$	0.016(1)
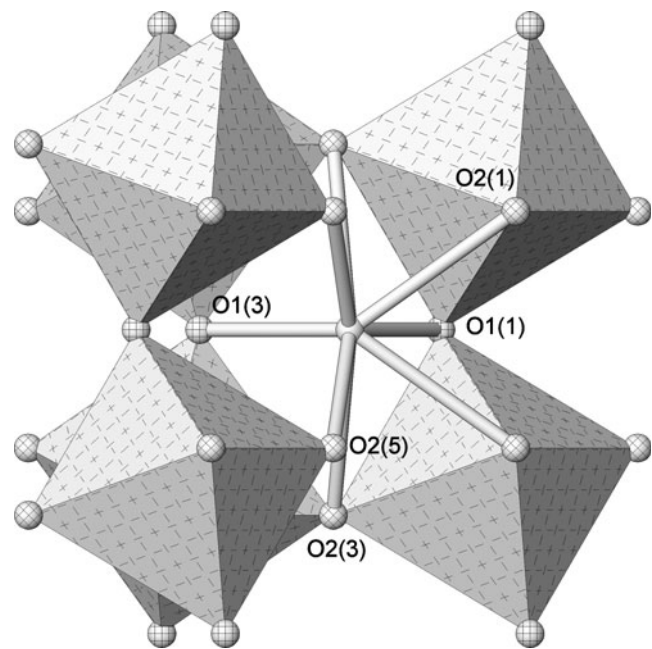
Fig. 7 8-fold coordination of the Sr cation (white) in $SrCe_{0.95}Yb_{0.05}O_\xi$ viewed down [011] with [100] vertical. Anion O1 is vertically/horizontally cross-hatched, anion O2 is diagonally cross-hatched

along the orthorhombic y direction, d_1, by a factor of 3.8 at 373K to nearly 5 at 1273K. These displacements are found to have a linear temperature-dependence as shown in Fig. 9
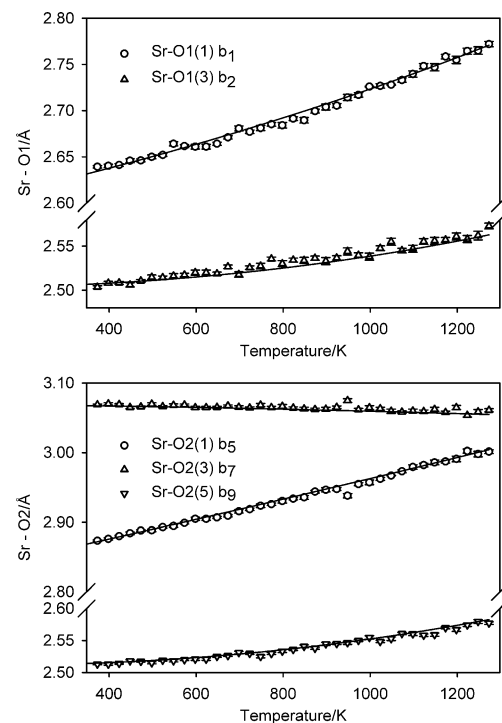
Fig. 8 The temperature-dependence of the five crystallographically independent Sr – O bonds in the SrO_8 polyhedron in $SrCe_{0.95}Yb_{0.05}O_\xi$. Full lines show the predicted temperature-dependent bond length variations based on the parameterisation of the symmetry-adapted basis-vector magnitudes in terms of low-order polynomials [36]
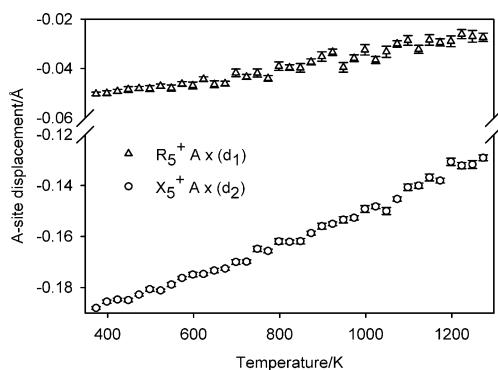
Fig. 9 The temperature variation of the A-site symmetry adapted basis vector magnitudes in $SrCe_{0.95}Yb_{0.05}O_\xi$

and are necessary to increase the length of the three short contacts from the chemically unreasonable values that the Sr^{2+} cation would exhibit if it was sited on its ideal position. The correlation in vibrational behaviour between Sr and O1 probably arises from this requirement. Even at the highest temperature measured, the three calculated cation - anion distances for the ideal cation position are less than those observed experimentally at 373 K. The magnitudes of both symmetry adapted basis vectors associated with the Sr cation decreases with increasing temperature, and extrapolate to zero magnitude at ~2213 K for d_1, and the physically unreasonable temperature of 3257 K for d_2, i.e. close to, and significantly above, the experimentally determined melting temperature of 2266 K [19].

Consideration of Fig. 8 shows that if the anti-phase tilt reduces in magnitude, the three intermediate contacts increase with temperature whilst the two longest bonds reduce. The increases in the intermediate bond lengths are approximately twice those of the three short bond lengths, at 1.50×10^{-4} $Å K^{-1}$ for Sr - O1, and 1.45×10^{-4} $Å K^{-1}$ for Sr - O2. The two longest bonds show a small decrease with temperature -1.1×10^{-5} $Å K^{-1}$. The displacements associated with the two octahedral tilt components, in-phase (ϕM) around [1, 0, 0], and anti-phase (ϕR) around [0, 1, 1], are shown in Fig. 10.
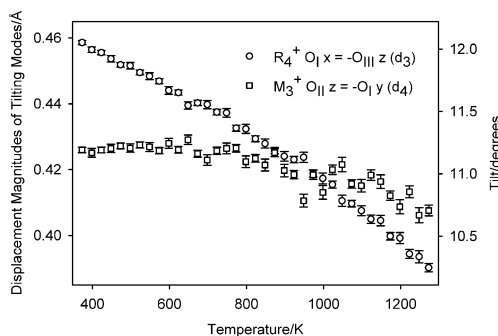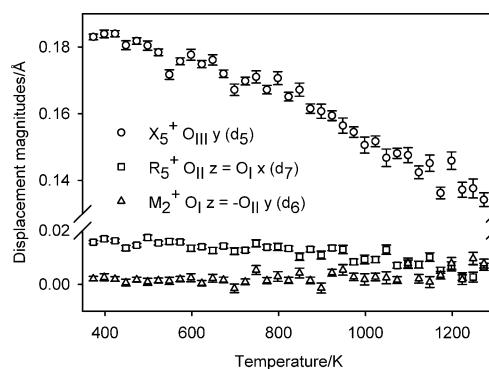
The total tilt angles can be calculated from the magnitudes of the displacements, d_3 or d_4, and the unit cell volume, V, as shown below

$$\phi R = \sqrt{2} \arctan\left(2\left(\frac{4}{V}\right)^{1/3} d_3\right)$$

$$\phi M = \arctan\left(2\left(\frac{4}{V}\right)^{1/3} d_4\right).$$

Note that the figure shows a single component of the anti-phase tilt and not the full tilt angle. The anti-phase tilt reduces 2.8° in 900 K, whilst the corresponding change in the in-phase tilt is, by comparison, much smaller. In single tilt systems, the critical exponent derived from the temperature-dependence of the tilt angle can in favourable circumstances be used to infer the thermodynamical nature of a phase transition e.g. the tricritical transitions $I4/mcm$ - $Pm\bar{3}m$ in $SrSnO_3$ [11] and $SrZrO_3$ [9]. Due to the potential coupling between the primary order parameters in $SrCe_{0.95}Yb_{0.05}O_\xi$, it is not possible to make any deductions with regard to either the nature or the presence of any potential higher temperature phase transitions from the temperature variations of the tilt displacements.

In addition to rigid unit rotation mediated by the symmetry adapted basis vectors that transform as the irreducible representations R_4^+ and M_3^+, the octahedra become distorted due to the effects of the modes that transform as the irreducible representations X_5^+, R_5^+ and M_2^+. Of these modes, consideration of Table 3 shows only X_5^+ (d_5) has a significant magnitude, whilst R_5^+ (d_7) is small, and indeed, it could be argued that M_2^+ (d_6) is zero within two – three estimated standard deviations. The principal effects of the mode with irreducible representation X_5^+ (d_5) are small deviations in the O1 – Ce – O2 bond angles from 90°, which are small. The amplitude associated

Fig. 10 The temperature dependence of the symmetry adapted basis vector magnitudes associated with octahedral tilting and the octahedral tilt angle magnitudes for single components of the primary order parameters in $SrCe_{0.95}Yb_{0.05}O_\xi$

Fig. 11 The temperature variation of the octahedral distortion modes in $SrCe_{0.95}Yb_{0.05}O_\xi$. The distortion of the octahedron is dominated by the mode that transforms as the irreducible representation X_5^+ whilst it can be argued that the mode M_2^+ has no structural significance within estimated standard deviation

with the mode M_2^+ is always found to be small in perovskites with space group *Pmcn* with the exception of Jahn-Teller distorted systems in which it is generally found to be large [35]. The displacement magnitudes for these three modes are shown in Fig. 11. By fitting the individual d_i to low order polynomials as a function of temperature (d_6: constant; d_2, d_7: linear; d_1, d_3, d_4, d_5: quadratic), and using the expressions of Knight [31] for the bond lengths in terms of d_i, the predicted temperature variations of the five symmetry-independent bond lengths in the SrO_8 polyhedron are shown in Fig. 8 as the full lines. The agreement between the observed and predicted temperature-dependence of the bond lengths is excellent in all five cases.

A more detailed discussion of this method of data analysis is given for the example of $CaTiO_3$ at low temperature by Knight [36].

4 Conclusions

Powder neutron diffraction has shown that the protonic conductor $SrCe_{0.95}Yb_{0.05}O_\xi$ remains orthorhombic, space group *Pmcn* ($a^+b^-b^-$) from 4.2K to 1273K with little evidence for the existence of any high-temperature structural phase transitions up to, and probably beyond, 1473K. The single crystal structure solution of $SrCeO_3$ made on a crystal grown from Bi_2O_3 flux at 1373 K made no mention of the need to correct data for the presence of twinning [37], and hence, from this observation, we can deduce that there are no phase transitions between 1273 K and 1373 K. However, HRTEM images of $SrCeO_3$ powder, synthesised at a maximum temperature of 1673 K, shows evidence of ferroelastic twin domains [38] which implies the existence of at least one structural phase transition between 1673 K and 1373 K that remains to be structurally characterized.

In contrast to its high-pressure behavior, which is dominated by octahedral bond length compression without changes in octahedral tilting [14], the high-temperature behavior results from rigid unit tilting without significant octahedral deformation. Knight et al. [14] concluded that this atypical behavior at high pressure for a $SrB^{IV}O_3$ perovskite and the lack of high-temperature structural phase transitions was due to the smallness of the perovskite tolerance factor coupled with the length of the Ce – O bond. In the light of the HRTEM observations, this conclusion requires further investigation by neutron powder diffraction at temperatures higher than 1373 K.

In keeping with observations made by Anderson concerning the nature of the dominant mantle mineral $MgSiO_3$ perovskite [26], $SrCe_{0.95}Yb_{0.05}O_\xi$ can be characterized as a Debye-like material, but in this case, and in contrast to $MgSiO_3$, there are two characteristic temperatures, the lower apparently related to the cation vibrations,

the higher to the anion vibrations. Self consistent values for these two temperatures have been found from the temperature-dependence of the atomic displacement parameters and by fitting calorimetric data to Debye models. Plausible Grüneisen parameters have been derived from the linear volume expansion coefficient and published heat capacity data, the values and their range are in agreement with literature values for other $A^{II}B^{IV}O_3$ perovskites.

Decomposition of the space group permitted structural degrees of freedom in terms of symmetry adapted basis vectors of the aristotype phase allows the structural variations in temperature to be examined in detail. The structural response to increasing temperature is dominated by the decreasing magnitudes of the octahedral tilting modes that transform as the irreducible representations R_4^+ and M_3^+, in conjunction with a reduction in magnitude of the A-site displacement mode X_5^+. Of the octahedral deformation modes, only the mode with irreducible representation X_5^+ has a significant magnitude and temperature dependence.

The competing structural processes in $SrCe_{0.95}Yb_{0.05}O_\xi$ that occur at high temperature (octahedral tilting without deformation), and at high pressure (octahedral deformation without tilting), would make a simultaneous high-temperature/high-pressure crystallographic investigation in these two thermodynamic variables an interesting study in structural frustration.

References

1. H. Iwahara, T. Esaka, H. Uchida, N. Maeda, Solid State Ionics **3/4**, 359 (1981)
2. K.-D. Kreuer, Th Dippel, Yu.M. Baikov, J. Maier, Solid State Ionics **86–88**, 613 (1996)
3. T. Norby, M. Wideroe, R. Glöckner, Y. Larring, Dalton Trans **19**, 3012 (2004)
4. K.S. Knight, Solid State Ionics **145**, 275 (2001)
5. K.S. Knight, Solid State Comm **112**, 73 (1999)
6. A. Saiki, Y. Seto, H. Seki, N. Ishizawa, M. Kato, N. Mizutani, Nippon Kagaku Kaishi **1**, 25 (1991)
7. K.S. Knight, N. Bonanos, Mater. Res. Bull. **30**, 347 (1995)
8. C.J. Howard, K.S. Knight, B.J. Kennedy, E.H. Kisi, J. Phys. Condens. Matter **12**, L677 (2000)
9. B.J. Kennedy, B.A. Hunter, J.R. Hester, Phys Rev B **65**, 224103 (2002)
10. B.J. Kennedy, K. Yamaura, E. Takayama-Muromachi, J Phys Chem Solid **65**, 1065 (2004)
11. M. Glerup, K.S. Knight, F.W. Poulsen, Mater. Res. Bull. **40**, 507 (2005)
12. B.J. Kennedy, C.J. Howard, B.C. Chakoumakos, Phys Rev B **60**, 2972 (1999)

13. B.J. Kennedy, C.J. Howard, G.J. Thorogood, J.R. Hester, J Solid State Chem **161**, 106 (2001)
14. K.S. Knight, W.G. Marshall, N. Bonanos, D.J. Francis, J. Alloys Compd. **394**, 131 (2005)
15. R.B. Von Dreele, A.C. Larson, Los Alamos National Laboratory Report LAUR 86–748 (1986)
16. R.A. Cowley, Phys Rev [Section A] **134**, 981 (1964)
17. S. Yamanaka, K. Kurosaki, T. Matsuda, S. Kobayashi, J. Alloys Compd. **352**, 52 (2003)
18. D.C. Wallace, *Thermodynamics of Crystals* (Wiley, New York, 1972)
19. E.H.P. Cordfunke, A.S. Booij, M.E. Huntelaar, J. Chem. Thermodyn. **30**, 437 (1998)
20. S. Loridant, G. Lucazeau, T. Le Bihan, J Phys Chem Solid **63**, 1983 (2002)
21. S. Yamanaka, K. Kurosaki, T. Maekawa, T. Matsuda, S. Kobayashi, M. Uno, J. Nucl. Mater. **344**, 61 (2005)
22. M. O'Keefe, B.G. Hyde, Acta Crystallographica **B33**, 3802 (1977)
23. J.R. Hester, C.J. Howard, B.J. Kennedy, R. Macquart, Aust. J. Chem. **55**, 543 (2002)
24. K.S. Knight, I.G. Wood, G.D. Price, J.A. Stuart, unpublished results
25. R.W. James, *The Optical Principles of the Diffraction of X-rays* (G. Bell and Sons Ltd., London, 1962)
26. B.T.M. Willis, A.W. Pryor, *Thermal Vibrations in Crystallography* (Cambridge University Press, Cambridge, 1975)
27. T.H.K. Barron, CINDAS Data Series on Materials Properties **I-4**, 1 (1998)
28. O.L. Anderson, Am. Mineral. **83**, 23 (1998)
29. K.S. Knight, Can. Mineral. **47**, 381 (2009)
30. K.S. Knight, Can. Mineral. **47**, 401 (2009)
31. K.S. Knight, Can. Mineral. **50**, 793 (2011)
32. C.J. Bradley, A.P. Cracknell, *The Mathematical Theory of Symmetry in Solids: Representation Theory for Point Groups and Space Groups* (Clarendon, Oxford, 1972)
33. J.M. Perez-Mato, D. Orobengoa, M.I. Aroyo, Acta Crystallographica **A66**, 558 (2010)
34. M.A. Carpenter, C.J. Howard, K.S. Knight, Z. Zhang, J. Phys. Condens. Matter **18**, 10725 (2006)
35. M.A. Carpenter, R.E.A. McKnight, C.J. Howard, K.S. Knight, Physical Review B **82**, 094101 (2010)
36. K.S. Knight, J. Alloys Compd. **509**, 6337 (2011)
37. J. Ranløv, K. Nielsen, J. Mater. Chem. **4**, 867 (1994)
38. G.C. Mather, F.M. Figueiredo, J. Romero de Paz, S. García-Martín, Inorg. Chem. **47**, 921 (2008)